ELSEVIER

International Journal of Heat and Fluid Flow 22 (2001) 473–479

International Journal of HEAT AND FLUID FLOW

www.elsevier.com/locate/ijhff

Solidification of circular Couette flow with viscous dissipation

Calvin Mackie [a], Carsie A. Hall [b,*], Judy A. Perkins [c]

[a] Department of Mechanical Engineering, Tulane University, New Orleans, LA 70118, USA
[b] Department of Mechanical Engineering, University of New Orleans, New Orleans, LA 70148, USA
[c] Department of Civil and Environmental Engineering, North Carolina A & T State University, Greensboro, NC 27411, USA

Received 12 July 2000; accepted 8 February 2001

Abstract

A semi-analytic solution is presented for the solidification of laminar circular Couette flow within a one-dimensional annular region with a rotating outer cylinder and stationary inner cylinder. Viscous dissipation in the liquid is taken into account. Closed-form expressions for the dimensionless temperature distribution in the solid and liquid regions, Nusselt number at the solid–liquid interface, dimensionless power and torque per unit length, dimensionless steady-state freeze front location, and dimensionless pressure distribution in the liquid are derived as a function of liquid-to-solid thermal conductivity ratio, Brinkman number, annulus radius ratio, and Stefan number, which is assumed to be small (<0.1) but non-vanishing. The instantaneous dimensionless solid–liquid interface location is determined using numerical integration. The results show that the power and torque requirements can increase by a factor of greater than seven for a thin-gap annulus (radius ratio >0.9). It is also shown that the size of the liquid region within the annular gap has a more controlling influence on the solidification rate at latter times (when the Brinkman number is small) while a Brinkman number of order unity has a dominant influence at earlier times.

Keywords: Circular Couette flow; Solidification; Viscous dissipation

1. Introduction

Fluid flows undergoing melting or solidification have been the subject of researchers due to potential applications in manufacturing processes (e.g., extrusion), fluidized beds of granular polymers, low-temperature viscometers, freeze blockage of liquids in pipes, circular and annular thrust bearings, and others (Pearson, 1976; Griffin, 1977; Cheung and Epstein, 1984; Slocum, 1992). These fluids typically exhibit Newtonian as well as non-Newtonian behavior (Bird et al., 1960; Luelf and Burmeister, 1996). Analytic or semi-analytic solutions to flows that exhibit Couette or Couette-like behavior such as purely shear-driven flows and near-wall turbulent flows with solid–liquid phase change have appeared sparsely in the literature. Researchers in crystal growth have investigated the effects of shear flows on directional solidification and have shown that the solidification rate plays a major role in determining the morphology of the solid–liquid interface and subsequent crystal formation (Huang et al., 1993).

While a majority of the investigations on parallel and circular shear flows with solid–liquid phase change have been experimental, few have been treated analytically. In fact, most analytical treatments have only been applied to semi-infinite domains. For example, Pearson (1976) presented a similarity solution and Griffin (1977) used an integral energy balance method to study two-dimensional, steady-state, non-Newtonian melting in the vicinity of a semi-infinite moving flat plate. Huang (1984) studied the transient Couette flow problem with viscous heating and used a combination of the similarity technique and Green's function to derive a closed-form solution for one-dimensional, Newtonian melting of a semi-infinite solid by a moving hot wall.

Taylor–Couette flow or flow between two infinitely long coaxial cylinders in relative motion has been investigated extensively to characterize the mechanisms that cause the instabilities that lead to the formation of Taylor vortices (Koschmieder, 1993). Schlichting (1968) showed that for tangential flow in an annulus (circular Couette flow) the transition Reynolds number reaches a minimum of about 50,000 when the dimensionless annulus thickness is about 0.05, corresponding to an annulus radius ratio of approximately 0.95, after which and before which the transition Reynolds number increases. The literature on Taylor–Couette flow and circular Couette flow is vast, particularly from the perspective of flow stability. Since flow stability is beyond the scope of the present work, a review of literature pertaining thereto is unwarranted as the Reynolds number in the present work will always be much less than the critical value, thus ensuring laminar flow.

In this paper, a semi-analytic solution is presented for one-dimensional freezing of laminar, circular Couette flow within a

* Corresponding author. Fax: +1-504-280-5539.
E-mail address: cahall@uno.edu (C.A. Hall).

0142-727X/01/$ - see front matter
PII: S0142-727X(01)00108-4

Notation

Br	Brinkman number
c	specific heat
h	convective heat transfer coefficient
h_{sf}	latent heat of fusion
k	thermal conductivity
Nu	Nusselt number
P	power
P'	power per unit length
p	dimensionless liquid pressure difference
$\wp$	liquid pressure
r	coordinate location
R_i	inner radius of annulus
R_o	outer radius of annulus
Ste	Stefan number
t	time
T	temperature
$\Im$	torque
$\Im'$	torque per unit length
u	velocity component in azimuthal direction
U	dimensionless velocity component in azimuthal direction

Greeks

α	thermal diffusivity
β	annulus radius ratio
δ	solid–liquid interface location
Δ	dimensionless solid–liquid interface location
γ	liquid-to-solid thermal conductivity ratio
η	dimensionless coordinate location
μ	dynamic viscosity
θ	dimensionless temperature
τ	dimensionless time or Fourier number
ω	angular speed of outer cylinder
ψ	solid-to-liquid thermal diffusivity ratio

Subscripts

l	referred to liquid region
m	referred to solid–liquid interface conditions
o	referred to outer cylinder or temperature on inner cylinder
s	referred to solid region
ss	referred to steady-state conditions

finite annular region with viscous dissipation in the low Stefan number limit. A rotating outer cylinder (with stationary inner cylinder) induces the shear-driven motion in the liquid region. Closed-form expressions for the quasi-steady temperature distributions in the solid and liquid regions are derived, and the instantaneous location of the solid–liquid interface is obtained through numerical integration. In addition, expressions for the Nusselt number at the solid–liquid interface, dimensionless power (and torque) per unit length, and pressure distribution in the liquid are all derived as a function of pertinent dimensionless parameters. It is shown that the semi-analytic solution reduces to a known classical result in the appropriate asymptotic limit.

2. Problem formulation

A one-dimensional region of thickness $(R_o - R_i)$ is illustrated in Fig. 1. The motion of the liquid in the annular region is assumed to be laminar and is shear-driven by an outer cylinder rotating at constant speed ω. The surface of the outer cylinder is assumed to be adiabatic, and the liquid is considered an incompressible, Newtonian fluid. The liquid is initially at or above its fusion temperature T_m according to a prescribed distribution $T_l = T_l(r, t < 0)$, and the inner cylinder is suddenly cooled isothermally to a temperature T_o, which is maintained below the liquid's fusion temperature. As a result, an axially symmetric freeze front propagates from the inner cylinder to the outer cylinder. Additional assumptions include: (1) all thermophysical properties are constant, (2) the flow field is unaffected by the growing solid layer, (3) the solid–liquid interface is sharp as phase change takes place at a distinct temperature, and (4) there is no motion due to density change (i.e., $\rho_s = \rho_l$).

After introducing the following dimensionless parameters into the one-dimensional momentum and energy equations, including viscous dissipation,

$$\eta = \frac{r}{R_o}, \quad \Delta = \frac{\delta}{R_o}, \quad U = \frac{u}{\omega R_o}, \quad \theta = \frac{T - T_o}{T_m - T_o},$$

$$\tau = \frac{t}{R_o^2/\alpha_s}, \quad p = \frac{\wp - \wp_m}{\rho_l \omega^2 R_o^2}, \quad Br = \frac{\mu_l (\omega R_o)^2}{k_l (T_m - T_o)},$$
$$\gamma = \frac{k_l}{k_s}, \quad \psi = \frac{\alpha_s}{\alpha_l}, \quad \beta = \frac{R_i}{R_o}, \quad Ste = \frac{c_s (T_m - T_o)}{h_{sf}}, \tag{1}$$

where τ is the dimensionless time or Fourier number, Br is the Brinkman number, β is the annulus radius ratio, and Ste is the Stefan number, the solution for the velocity distribution in the liquid region is derived as (assuming no-slip conditions at the solid–liquid interface)

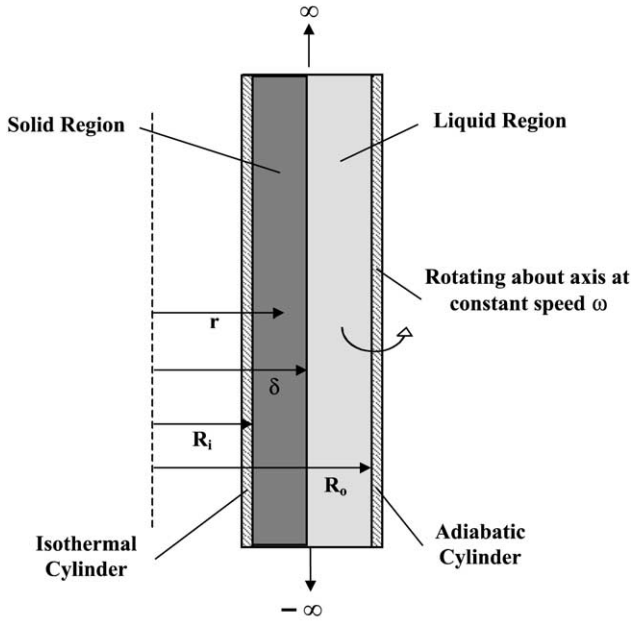

Fig. 1. Schematic model and nomenclature of circular Couette flow region undergoing solidification with rotating outer cylinder and stationary inner cylinder.

$$U(\eta,\tau)=\frac{1}{\eta}\left\{\frac{\eta^2-[\Delta(\tau)]^2}{1-[\Delta(\tau)]^2}\right\}. \tag{2}$$

Subsequently, $U(\eta,\tau)$ is used to determine the dimensionless temperature distribution in the liquid region via the dimensionless energy equation

$$\psi\frac{\partial\theta_l}{\partial\tau}=\frac{1}{\eta}\frac{\partial}{\partial\eta}\left(\eta\frac{\partial\theta_l}{\partial\eta}\right)+Br\left[\eta\frac{\partial}{\partial\eta}\left(\frac{U}{\eta}\right)\right]^2 \tag{3}$$

or, by substituting Eq. (2)

$$\psi\frac{\partial\theta_l}{\partial\tau}=\frac{1}{\eta}\frac{\partial}{\partial\eta}\left(\eta\frac{\partial\theta_l}{\partial\eta}\right)+\frac{4Br\Delta^4}{\left(1-\Delta^2\right)^2}\frac{1}{\eta^4}. \tag{4}$$

Eq. (4) is subject to the initial condition

$$\theta_l(\eta,\tau=0)=\frac{Br\beta^4}{\left[1-\beta^2\right]^2}\left[\ln\left(\frac{\beta^2}{\eta^2}\right)+\left(\frac{1}{\beta^2}-\frac{1}{\eta^2}\right)\right]+1 \tag{5}$$

and boundary conditions

$$\left.\frac{\partial\theta_l}{\partial\eta}\right|_{\eta=1}=0 \text{ and } \theta_l(\eta=\Delta^+,\tau)=1. \tag{6}$$

Integrating the quasi-steady form of Eq. (4), subject to Eq. (6), results in

$$\theta_l(\eta,\tau)=\frac{Br[\Delta(\tau)]^4}{\left\{1-[\Delta(\tau)]^2\right\}^2}\left[\ln\left\{\frac{[\Delta(\tau)]^2}{\eta^2}\right\}+\left\{\frac{1}{[\Delta(\tau)]^2}-\frac{1}{\eta^2}\right\}\right]+1. \tag{7}$$

The transient term in Eq. (4) is neglected due to the low value of the liquid-side Stefan number, which is explained as follows. First, it is observed that the maximum liquid temperature $T_{l\max}$ is at the adiabatic boundary ($\eta=1$), and occurs at steady state, which reduces Eq. (7) to

$$\theta_{l\max}=\frac{Br\Delta_{ss}^4}{\left(1-\Delta_{ss}^2\right)^2}\left[2\ln\Delta_{ss}+\frac{1}{\Delta_{ss}^2}-1\right]+1, \tag{8}$$

where $\theta_{l\max}$ corresponds to θ_l evaluated at $T_{l\max}$, which occurs under steady-state conditions. Accordingly, the liquid-side Stefan number is defined as

$$Ste_l=\frac{c_l(T_{l\max}-T_m)}{h_{sf}}. \tag{9}$$

Then, using the definition of the solid-side Stefan number (Eq. (1)), the ratio of liquid-to-solid-side Stefan number can be expressed as

$$\frac{Ste_l}{Ste_s}=\frac{c_l}{c_s}\left(\frac{T_{l\max}-T_m}{T_m-T_o}\right)=\frac{c_l}{c_s}\left(\frac{T_{l\max}-T_o}{T_m-T_o}-1\right)=\frac{c_l}{c_s}(\theta_{l\max}-1). \tag{10}$$

Using Eq. (8), this ratio reduces to

$$\frac{Ste_l}{Ste_s}=Br\left(\frac{c_l}{c_s}\right)\left[\frac{\Delta_{ss}^4}{\left(1-\Delta_{ss}^2\right)^2}\left(2\ln\Delta_{ss}+\frac{1}{\Delta_{ss}^2}-1\right)\right]. \tag{11}$$

Through the use of L'Hospital's rule, the quantity within the brackets in Eq. (11) approaches a maximum value of 1/2 as Δ_{ss} approaches its limiting value of unity. This is corroborated in Fig. 2, which is a plot of the bracketed term in Eq. (11) as a function of Δ_{ss}. Note that this bracketed term is exactly $(\theta_{l\max}-1)/Br$ and will always be less than unity. In this

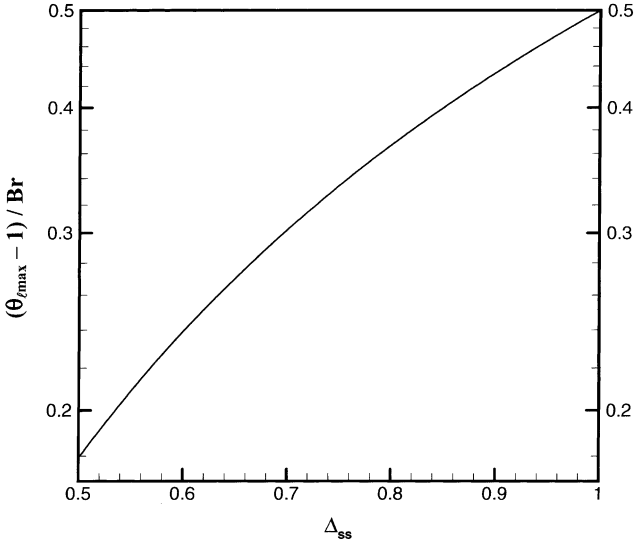

Fig. 2. Graphical illustration of the bracketed term in Eq. (11) as a function of dimensionless steady-state freeze front location.

study, the Brinkman number will be of order unity or several orders of magnitude less than unity while the liquid-to-solid specific heat ratio will remain of order unity. As a result, the liquid-side Stefan number will always be of the same order of magnitude or less than the solid-side Stefan number. In what follows, the solid-side Stefan number is assumed to be small but non-vanishing, which also applies to the liquid-side Stefan number. Therefore, the sensible heat contributions on both the solid and liquid sides are neglected. Alexiades and Solomon (1993) show that when the Stefan number is less than about 10^{-1}, the quasi-steady approximation gives excellent results.

The dimensionless one-dimensional temperature distribution in the solid region is described by the heat diffusion equation, expressed in dimensionless form as

$$\frac{\partial\theta_s}{\partial\tau}=\frac{1}{\eta}\frac{\partial}{\partial\eta}\left(\eta\frac{d\theta_s}{d\eta}\right) \tag{12}$$

subject to the initial condition

$$\theta_s(\eta,\tau=0)=\frac{Br\beta^4}{\left[1-\beta^2\right]^2}\left[\ln\left(\frac{\beta^2}{\eta^2}\right)+\left(\frac{1}{\beta^2}-\frac{1}{\eta^2}\right)\right]+1 \tag{13}$$

and boundary conditions

$$\theta_s(\eta=\beta,\tau)=0 \quad \text{and} \quad \theta_s(\eta=\Delta^-,\tau)=1. \tag{14}$$

The corresponding Stefan condition is given by (Alexiades and Solomon, 1993)

$$\left.\frac{\partial\theta_s}{\partial\eta}\right|_{\eta=\Delta^-}-\gamma\left.\frac{\partial\theta_l}{\partial\eta}\right|_{\eta=\Delta^+}=\frac{1}{Ste}\frac{d\Delta}{d\tau} \tag{15}$$

and an approximate analytical solution to the present problem is possible when solidification is assumed to progress in a quasi-steady manner, which is valid in the limit of low Stefan numbers. Therefore, the solution to the quasi-steady form of Eq. (12), subject to Eq. (14), is

$$\theta_s(\eta,\tau)=\frac{\ln[\eta/\beta]}{\ln[\Delta(\tau)/\beta]}. \tag{16}$$

As a result, the Stefan condition becomes

$$\frac{1}{\Delta \ln(\Delta/\beta)} - \frac{2\gamma Br\Delta}{1-\Delta^2} = \frac{1}{Ste}\frac{\mathrm{d}\Delta}{\mathrm{d}\tau}, \tag{17}$$

which is separated and integrated as follows:

$$\int_{\beta}^{\Delta} \frac{\Delta'\left(1-\Delta'^2\right)\left[\ln\left(\Delta'/\beta\right)\right]}{1-\Delta'^2-2\gamma Br\Delta'^2\ln\left(\Delta'/\beta\right)}\mathrm{d}\Delta' = Ste\int_{0}^{\tau}\mathrm{d}\tau'. \tag{18}$$

The left-hand side of Eq. (18) is subsequently integrated numerically using a known technique (e.g., Composite Trapezoidal Rule) to obtain the instantaneous dimensionless freeze front location as a function of the dimensionless parameters γ, Br, β, and Ste.

Note that as the freeze front moves towards the outer cylinder, the amount of viscous heating increases due to increasing shear stress, which increases the liquid-side heat flux at the solid–liquid interface. As a result, the solidification rate decreases and eventually reaches zero (steady-state) when the liquid-side heat flux exactly balances the solid-side heat flux. This steady-state condition can be expressed mathematically as

$$\frac{1}{\ln(\Delta_{ss}/\beta)} - \frac{2\gamma Br\Delta_{ss}^2}{1-\Delta_{ss}^2} = 0 \Rightarrow \frac{\left(1-\Delta_{ss}^2\right)}{\Delta_{ss}^2\ln(\Delta_{ss}/\beta)} = 2\gamma Br. \tag{19}$$

Figure 3 is a convenient graphical representation of Eq. (19), which is shown for selected annulus radius ratios. This figure shows the permissible range, with respect to the steady-state freeze front location, of the product of the liquid-to-solid thermal conductivity ratio and Brinkman number.

Within the framework of the present model, there are some other quantities of interest, namely the Nusselt number at the freeze front, derived to be

$$\begin{aligned} Nu &= \frac{hR_o}{k_l} = \frac{q''R_o}{k_l(T_{max}-T_m)} = (\theta_{l\max}-1)^{-1}\left.\frac{\partial\theta_l}{\partial\eta}\right|_{\eta=\Delta^+} \\ &= \frac{2Br\Delta}{1-\Delta^2}(\theta_{l\max}-1)^{-1} \Rightarrow Nu \\ &= \frac{2\Delta}{1-\Delta^2}\left[\frac{\left(1-\Delta_{ss}^2\right)^2}{\Delta_{ss}^4\left(2\ln\Delta_{ss}+1/\Delta_{ss}^2-1\right)}\right], \end{aligned} \tag{20}$$

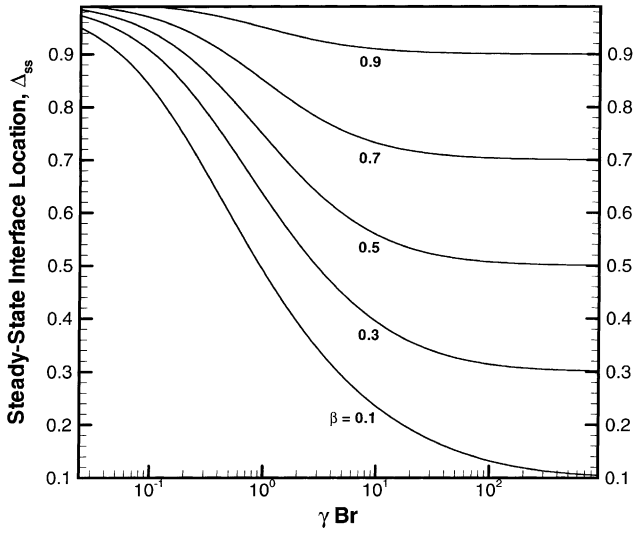

Fig. 3. Variation of dimensionless steady-state solid–liquid interface location as a function of the product of liquid-to-solid thermal conductivity ratio and Brinkman number for selected annulus radius ratios.

which is explicitly independent of Br. Therefore, with this definition, the Nusselt number derived above [Eq. (20)] can be used to characterize heat transfer problems with or without viscous dissipation ($Br = 0$). Furthermore, the power (per unit length L) required to maintain the outer cylinder in motion at constant angular speed, which is a function of the shear stress on the outer cylinder, is of interest and is given by

$$\begin{aligned} P &= \omega R_o\int\tau_{r=R_o}\mathrm{d}A = \omega R_o(2\pi R_o L)\mu\left[r\frac{\partial}{\partial r}\left(\frac{u}{r}\right)\right]_{r=R_o} \\ &\Rightarrow P' = \frac{P}{L} = 2\pi\omega^2R_o^2\mu\left[\eta\frac{\partial}{\partial\eta}\left(\frac{U}{\eta}\right)\right]_{\eta=1} \Rightarrow \frac{P'}{2\pi\mu\omega^2R_o^2} \\ &= \frac{2\Delta^2}{1-\Delta^2}. \end{aligned} \tag{21}$$

It is observed that Eqs. (20) and (21) are related by

$$\frac{\Delta Nu(\theta_{l\max}-1)}{Br} = \frac{P'}{2\pi\mu\omega^2R_o^2} = \frac{2\Delta^2}{1-\Delta^2}. \tag{22}$$

Another quantity that is often of interest is the torque, $\Im$, required on the outer cylinder, which is related to the power by

$$P = \Im\omega \text{ or } P' = \Im'\omega \tag{23}$$

and the dimensionless torque per unit length results

$$\frac{\Im'}{2\pi\mu\omega R_o^2} = \frac{2\Delta^2}{1-\Delta^2}, \tag{24}$$

which is the exact form of the expression found in Koschmieder (1993) and Schlichting (1968), only the inner boundary is not fixed but is a function of time according to $\Delta(\tau)$.

Lastly, it is important to characterize the changes in the pressure distribution in the annular region due to motion of the freeze front. Therefore, the pressure distribution in the liquid region is described by a radial-direction momentum balance, expressed in dimensionless form as

$$\frac{\partial p}{\partial\eta} = \frac{U^2}{\eta}, \tag{25}$$

which, physically, is a balance between the radial pressure force and the opposing centrifugal force. The dimensionless boundary condition for pressure is taken at the solid–liquid interface where thermodynamic equilibrium conditions are assumed to prevail. As a result, the solution to Eq. (25) is given by

$$p(\eta,\tau) = \frac{1}{2}\left(\frac{\Delta}{1-\Delta^2}\right)^2\left[\left(\frac{\eta}{\Delta}\right)^2 - \left(\frac{\Delta}{\eta}\right)^2 + \ln\left(\frac{\Delta}{\eta}\right)^4\right], \tag{26}$$

which is obtained by arbitrarily taking the dimensionless pressure difference at the freeze front p_m to be zero.

3. Results and discussion

The integral given by Eq. (18) reduces to a known classical form when the liquid medium is everywhere stationary ($Br \to 0$), which when integrated results in

$$\frac{1}{2}\left[\Delta^2\ln(\Delta/\beta) - \frac{1}{2}\left(\Delta^2-\beta^2\right)\right] = Ste\cdot\tau, \tag{27}$$

which is exactly the non-dimensional form of the quasi-steady solution to outward freezing of a fluid in an annulus due to imposed temperature on the inner cylinder found in Alexiades and Solomon (1993). In Fig. 4, the solution obtained by numerically integrating the left-hand side of Eq. (18) by the Composite Trapezoid Rule (Fausett, 1999) is superimposed on

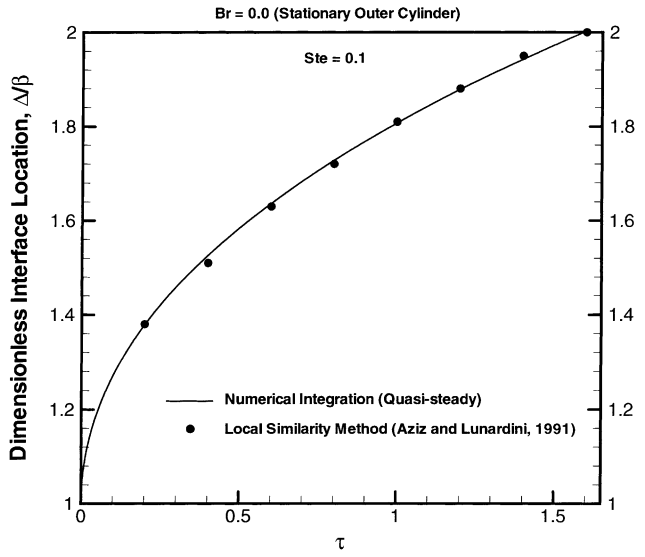

Fig. 4. Comparison of the solution obtained by numerical integration (quasi-steady conditions) to the local similarity solution of Aziz and Lunardini (1991) for the temporal variation of the dimensionless freeze front location at $Br = 0$ (stationary outer cylinder) and $Ste = 10^{-1}$.

the local similarity solution of Aziz and Lunardini (1991). This exercise is performed to gain confidence in and to ensure accuracy of the numerical integration technique. The Stefan number is fixed at 0.1 and the Brinkman number is held at zero, which corresponds to a stationary outer cylinder and no corresponding circular shear flow. As shown in the figure, the solution obtained by numerical integration for the instantaneous freeze front location gives excellent results. The maximum error is less than one percent. Furthermore, the local similarity method used by Aziz and Lunardini (1991) for outward cylindrical freezing with constant wall temperature showed accurate results when compared to the numerical solution obtained by Bell (1979).

The time variation of the instantaneous normalized dimensionless freeze front location is shown in Fig. 5 for Brinkman number of unity ($Br = 1$) and for annulus radius ratios of $\beta = 0.5$ (wide-gap annulus) and $\beta = 0.9$ (thin-gap annulus). The normalization is with respect to the steady-state dimensionless freeze front location, which is calculated to be $\Delta_{ss} = 0.8405$ and 0.9743 for radius ratios of 0.5 and 0.9, respectively. The variation of the instantaneous Nusselt number at the freeze front is also plotted in the figure. In this paper, the time that it takes from the start of solidification ($Ste \cdot \tau = 0$) to immobilization of the freeze front at steady-state conditions will be called the neutral freeze time (NFT) ($\mathrm{NFT} = Ste \cdot \tau_{\mathrm{NFT}}$). A significant effect of circular shear flow and annular gap on the NFT can be observed in Fig. 5. The presence of circular shear flow extends the NFT due to viscous dissipation in the liquid region, which results in higher temperature gradients in the liquid, particularly at the solid–liquid interface. In fact, the NFT is extended from 1.591×10^{-1} to 6.147×10^{-1} (a factor increase of about 3.86) for $\beta = 0.5$ while for $\beta = 0.9$, the NFT is increased from 5.17×10^{-3} to 1.23×10^{-2} (a factor increase of about 2.4) when compared to results obtained for the stationary outer cylinder case ($Br = 0$). The root cause of the extended NFT is due to the sharp rise and subsequent flattening of the interface Nusselt number, which is attributed to an increase in viscous heating as the interface approaches its steady-state location. In the figure, the Nusselt number increases from its initial value of about 3.38 to its steady-state value of approximately 14.5 (a factor increase of about 4.2) and from 19.75 to 70.4 (a factor increase of about 3.5) for radius ratios of 0.5 and 0.9, respectively.

Figure 6 illustrates the instantaneous normalized dimensionless power per unit length required to maintain the rotation of the outer cylinder at constant speed for Brinkman number of unity and for selected radius ratios. The normalization is with respect to the initial power per unit length just before freezing starts. This normalization is performed so that the effect of solidification on the power characteristics can be directly observed. Superimposed on the figure is the dimensionless power per unit length. It is observed that the power requirement increases by a factor of up to approximately 7.2 for a radius ratio of 0.5 while the power requirement increases by a factor of up to about 3.85 at a radius ratio of 0.9. However, note that the actual (not normalized) dimensionless

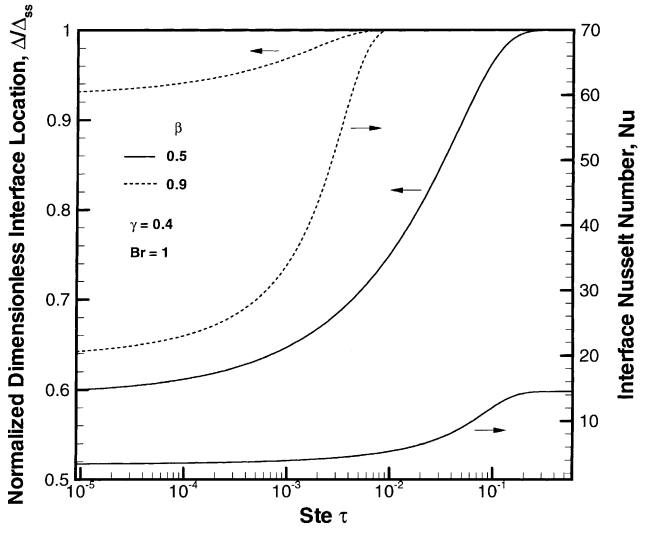

Fig. 5. Temporal variation of the ratio of instantaneous dimensionless freeze front location to steady-state dimensionless freeze front location and Nusselt number at the freeze front for selected radius ratios.

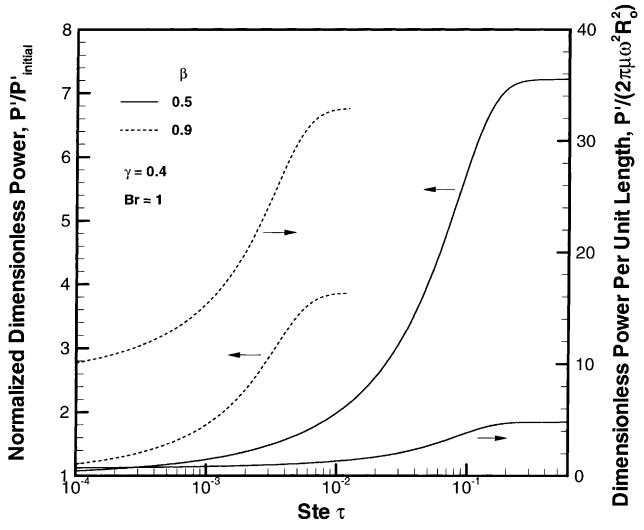

Fig. 6. Temporal variation of the ratio of instantaneous power per unit length to initial power per unit length for selected radius ratios.

power per unit length is higher throughout the entire freeze period for the thin-gap annulus ($\beta = 0.9$) than for the wide-gap annulus ($\beta = 0.5$), as expected. In fact, the dimensionless power per unit length reaches a maximum value of about 4.8 for $\beta = 0.5$ and a maximum of approximately 32.89 for $\beta = 0.9$.

The instantaneous dimensionless maximum liquid temperature and pressure, both of which are located on the adiabatic boundary, are plotted in Fig. 7 for Brinkman number of unity and for radius ratios of 0.5 and 0.9. It is first observed that the temperature increases and the pressure decreases as the freeze front progresses. This is observed for both representative radius ratios. In fact, the temperature and pressure profiles are direct geometric reflections of each other. However, the reflection is more pronounced for the wide-gap annulus ($\beta = 0.5$). Note that these reflections agree with one's physical intuition regarding the temperature–pressure relationship among liquids under centrifugal forces. That is, as the liquid's temperature is raised due to increased viscous dissipation as the freeze front progresses, the liquid's density is lowered, resulting in smaller centrifugal forces. This, in turn, leads to smaller opposing radial pressure forces. In the figure, it is observed that the dimensionless maximum temperature increases from about 1.18 to approximately 1.4 and the dimensionless maximum liquid pressure decreases from approximately 2.17×10^{-1} to about 5.77×10^{-2} (a factor decrease of about 3.76) for a radius ratio of 0.5. On the other hand, for a radius ratio of 0.9, the dimensionless maximum temperature increases from about 1.43 to approximately 1.48 and the dimensionless maximum liquid pressure decreases from approximately 3.5×10^{-2} to about 9.87×10^{-3} (a factor decrease of about 3.5).

With the annulus radius ratio fixed at 0.5 and the Brinkman number held at unity, the velocity and pressure distributions across the annular gap before solidification starts and after the NFT is reached are shown in Fig. 8. The figure shows that for the wide-gap annulus, the initial velocity distribution is non-linear, as expected. However, the final velocity distribution is linear since the progressing freeze front makes the liquid gap smaller, which is the limiting case of planar Couette flow. This behavior is not observed with the pressure distribution. In fact, the pressure distribution remains non-linear, initially and after the NFT is reached. In either case, the dimensionless velocity

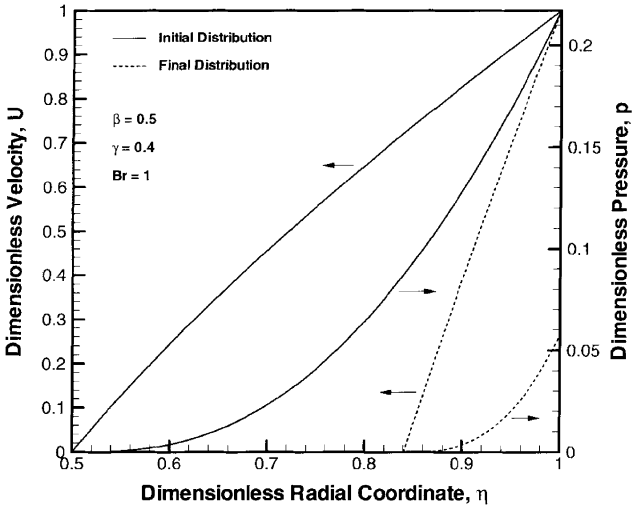

Fig. 8. Initial and final spatial distributions of velocity and pressure across the liquid region.

increases from zero at the solid–liquid interface to its maximum value of unity at the outer cylinder whereas the dimensionless pressure increases from zero at the freeze front to its maximum initial value of 2.17×10^{-1} and maximum final value of 5.77×10^{-2}.

Figure 9 illustrates the effect of Brinkman number ($Br = 0.01$, 0.1, and 1) on the dimensionless solidification rate and Nusselt number at the freeze front for a fixed annulus radius ratio of 0.5. It is observed that for smaller Brinkman numbers ($Br = 0.01$ and 0.1), there is no significant difference (except for $Br = 1$) in the freeze rates, except at latter times when the Nusselt number increases sharply (especially for $Br = 0.01$) due to close proximity of the solid–liquid interface to the outer cylinder. This is important because the annular liquid gap appears to be the controlling parameter in terms of characterizing heat transfer at the solid–liquid interface. Note that in all cases, the freeze rate decreases throughout the entire freeze period and eventually reaches zero when steady state is reached. Another observation is that increasing the Brinkman

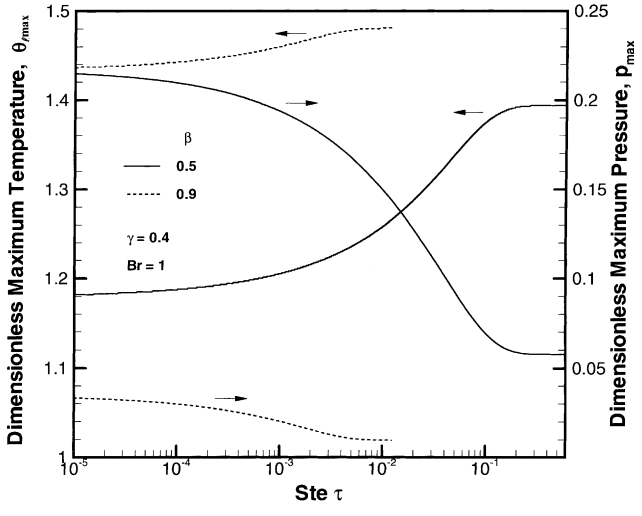

Fig. 7. Temporal variation of the maximum liquid temperature and pressure for selected radius ratios.

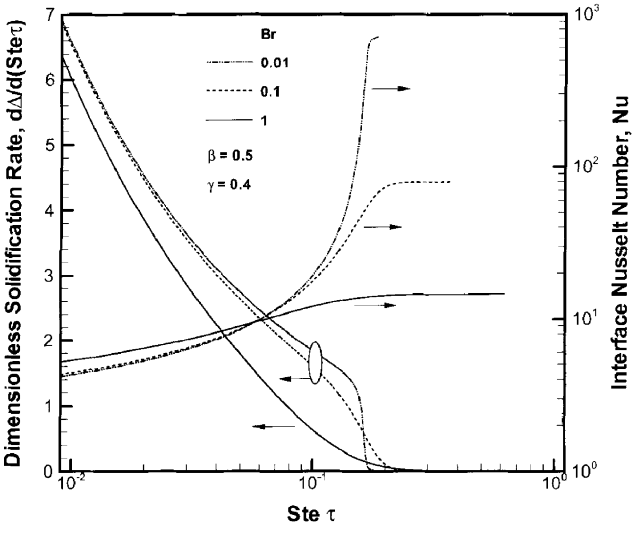

Fig. 9. Temporal variation of the dimensionless solidification rate and Nusselt number at the freeze front for selected Brinkman numbers.

number increases the NFT since the increased viscous heating slows the motion of the interface earlier in the freeze cycle when the liquid gap is larger. In fact, for $Br = 1$, the interface Nusselt number is larger than the interface Nusselt numbers corresponding to $Br = 0.01$ and 0.1 up until around $Ste \cdot \tau \approx 6 \times 10^{-2}$, after which the interface Nusselt number corresponding to $Br = 1$ begins to flatten out to its maximum value of approximately 15. On the other hand, after about $Ste \cdot \tau \approx 6 \times 10^{-2}$, the interface Nusselt numbers corresponding to $Br = 0.01$ and 0.1 increase sharply until they start to level off to their maximum values of about 712 and 80, respectively.

4. Conclusions

A semi-analytic solution was presented for one-dimensional freezing of laminar Couette flow within an annular region with a rotating outer cylinder and stationary inner cylinder. The effect of viscous dissipation in the liquid was taken into account. Analytical expressions for the dimensionless temperature distribution in the solid and liquid regions, Nusselt number at the freeze front, dimensionless power and torque per unit length, dimensionless steady-state freeze front location, and dimensionless pressure distribution in the liquid were derived as a function of liquid-to-solid thermal conductivity ratio, Brinkman number, annulus radius ratio, and Stefan number. The instantaneous dimensionless freeze front location was determined using numerical integration. The solution demonstrated that a known classical result could be obtained in the appropriate asymptotic limit. The results also showed that the power and torque requirements increased by a factor of up to seven due to the solidifying circular Couette flow. It was also shown that the presence of viscous dissipation extended the freeze time by almost a factor of four for the wide-gap annulus and a factor of almost 2.5 for the thin-gap annulus.

References

Alexiades, V., Solomon, A.D., 1993. Mathematical Modeling of Melting and Freezing Processes. Hemisphere, Washington, DC.

Aziz, A., Lunardini, V.J., 1991. Application of local similarity method to nonsimilar conduction controlled freezing problems. Int. Comm. Heat Mass Transfer 18, 813–822.

Bell, G.E., 1979. Solidification of a liquid about a cylindrical pipe. Int. J. Heat Mass Transfer 22, 1681–1685.

Bird, R.B., Stewart, W.E., Lightfoot, E.N., 1960. Transport Phenomena. Wiley, New York.

Cheung, F.B., Epstein, M., 1984. Solidification and melting in fluid flow. In: Mujumdar, A., Mashelkar, R.A. (Eds.), Advances in Transport Processes, vol. 3. Wiley, New York, pp. 35–117.

Fausett, L.V., 1999. Applied Numerical Analysis Using Matlab®. Prentice Hall, Upper Saddle River, NJ.

Griffin, O.M., 1977. An integral energy-balance model for the melting of solids on a hot moving surface, with application to the transport processes during extrusion. Int. J. Heat Mass Transfer 20, 675–683.

Huang, S.C., 1984. Melting of semi-infinite region with viscous heating. Int. J. Heat Mass Transfer 27, 1337–1343.

Huang, T., Liu, S., Yang, Y., Lu, D., Zhou, Y., 1993. Coupling of couette flow and crystal morphologies in directional freezing. J. Crystal Growth 128, 167–172.

Koschmieder, E.L., 1993. Benard Cells and Taylor Vortices. Cambridge University Press, Cambridge.

Luelf, W.C., Burmeister, L.C., 1996. Viscous dissipation effect on pressure gradient for laminar flow of a non-newtonian liquid through a duct of subfreezing wall temperature. J. Heat Transfer 118, 973–976.

Pearson, J.R.A., 1976. On the melting of solids near a hot moving interface, with particular reference to beds of granular polymers. Int. J. Heat Mass Transfer 19, 405–411.

Schlichting, H., 1968. Boundary-Layer Theory, sixth ed. McGraw-Hill, New York.

Slocum, A.H., 1992. Precision Machine Design. Prentice-Hall, Englewood Cliffs, NJ.